Light Metals 2013 *Edited by: Barry Sadler*
TMS (The Minerals, Metals & Materials Society), 2013

Light Metals 2013

ELECTRODE TECHNOLOGY FOR ALUMINUM PRODUCTION

Inert Anodes, Cell Materials and Alternative Processes

SESSION CHAIR
Elaine Sum
Rio Tinto Alcan
Voreppe, France

Light Metals 2013 *Edited by: Barry Sadler*
TMS (The Minerals, Metals & Materials Society), 2013

Mechanically alloyed Cu-Ni-Fe-Y material as inert anode for Al production

V. Ouvarov-Bancalero[1], D. Guay[1] and L. Roué[1]
[1]INRS-Énergie Matériaux Télécommunication; 1650 Boulevard Lionel-Boulet; Varennes, Québec, J3X 1S2, Canada

Keywords: aluminum electrolysis, inert anode, Cu-Ni-Fe-Y alloy, ball milling, low-temperature electrolyte

Abstract

In our previous works, we identified the mechanically alloyed $Cu_{65}Ni_{20}Fe_{15}$ compound as a promising inert anode material for Al production in low temperature (700°C) KF-AlF_3 electrolyte. However, further work was required for improving its corrosion resistance. For that purpose, $(Cu_{65}Ni_{20}Fe_{15})_{100-x}Y_x$ materials were prepared by ball milling, consolidated to form dense electrodes and then evaluated as inert anodes for aluminum production. Their morphological, structural and chemical characteristics were studied at different stages of their preparation and after 20 h of electrolysis. The key role played by the element Y on the electrode's corrosion resistance is highlighted.

Introduction

During the last decade, the aluminum producers have consented to major efforts (plant modernization, process upgrade, strict control over processes) for reducing the environmental impact of their operations. However, their emissions of greenhouse gas are still high (from 2.5 to 15 tonnes of CO_2-equivalent per tonne of produced Al, depending on its geographic origin) **[1]**.

A long-term objective of the aluminum industry is to substitute the consumable carbon anodes by inert materials, in order to release O_2 instead of CO_2 during the electrolysis process. Among the possible inert materials (metals, ceramics and cermets) **[2,3]**, metallic anodes appear to be the most promising candidates because they offer high electrical conductivity, excellent thermal shock resistance, mechanical robustness, ease of manufacture and simplicity of electrical connection to the current lead **[4]**. In addition, the use of a low temperature KF-AlF_3-based electrolyte having a high alumina solubility (~5 wt.% at 700°C) is advantageous, especially for metallic inert anodes because the decrease of the electrolyte temperature has a major positive impact on their corrosion rate **[5-7]**. However, up to date, no viable metallic anodes have been found in long-term and large scale electrolysis conditions.

Among the large choice of metallic materials, Cu-Ni-Fe based alloys present promising properties as inert anodes in low-temperature (750°C) NaF-AlF_3 electrolyte **[8]**. However, such materials suffer from selective corrosion due to their bi-phasic structure, with one Cu-rich phase and one Fe-rich phase. During electrolysis, the Fe-rich phase is preferentially attacked leading to the creation of iron fluoride tunnels that decrease the corrosion resistance of the alloy **[9]**. We have recently shown that monophasic Cu-Ni-Fe alloys can be obtained by mechanical alloying over a large composition range **[10]**. Best results were obtained with the $Cu_{65}Ni_{20}Fe_{15}$ (wt.%) anode, which presents good corrosion resistance in low temperature KF-AlF_3-based electrolyte, resulting in the production of Al with a purity of 99.3%. Further improvement in the anode corrosion resistance was obtained by milling the $Cu_{65}Ni_{20}Fe_{15}$ alloy powder under oxygen atmosphere during an appropriate time **[11]**. Best results were obtained with the Cu-Ni-Fe-O anode containing 1.4 wt.% O. For this anode composition, the cell voltage is low and stable and the produced Al has a purity of 99.8%. During Al electrolysis, the surface of the electrode is covered by a protective $NiFe_2O_4$-rich outer scale. This layer reduces the migration of copper to the electrode surface. Since the solubility $NiFe_2O_4$ in the cryolitic bath is very low compared to that of Cu_2O, the electrode presents good corrosion resistance with an estimated dissolution rate of 0.8 cm $year^{-1}$ **[11]**.

In the present study, the influence of yttrium addition on the corrosion resistance of the $Cu_{65}Ni_{20}Fe_{15}$ anode was investigated. The choice of yttrium as an additive element is motivated by its well-known ability to improve high-temperature corrosion resistance of various alloys in oxidising environments **[12]**. The morphological, structural and chemical characteristics of mechanically alloyed $Cu_{65}Ni_{20}Fe_{15}$ and $(Cu_{65}Ni_{20}Fe_{15})_{95}Y_5$ materials were compared at different stages of their preparation and after 20 h of electrolysis in low temperature (700°C) KF-AlF_3 electrolyte.

Experimental

The $Cu_{65}Ni_{20}Fe_{15}$ and $(Cu_{65}Ni_{20}Fe_{15})_{95}Y_5$ (in wt.%) compounds were prepared from pure Cu, Ni, Fe and Y powders (Cu purity ≥ 99.5%, Ni, Fe purity ≥ 99.9, -325 mesh and Y purity ≥ 99.9, -40 mesh). These materials were prepared by high-energy ball milling using a Spex 8000 laboratory mill. The powder mixture was introduced into a hardened steel vial (capacity of 55 mL) with three hardened steel balls (two of diameter 14 mm and one of 11 mm). The ball-to-powder mass ratio (BPR) was 2:1. The vial was loaded and sealed under argon atmosphere and the milling duration was fixed at 10 h. 0.5 wt.% of stearic acid was added to the initial powder mixture as a process control agent to prevent excessive cold welding. The milling yields, defined as the ratio of the powder masses after and before milling, were ≥ 90%. The composition of the end-products (determined by energy dispersive X-ray analysis) was in accordance with their nominal composition except for a slight Fe enrichment (1-2 wt.%) due to the erosion of the steel vial and balls upon milling.

Powder consolidation was carried out to obtain dense disc samples for the electrolysis tests. The as-milled powder was firstly sieved to select only the powder fraction with a particle size of 20 to 75 µm. This sieved powder was placed in a quartz cylinder preform and heated from room temperature to 1000°C under Ar + H_2 (95/5) atmosphere (softening treatment). The resulting sample was cold pressed at 26 tons cm^{-2} for 10 min and then sintered at 1000°C under Ar + H_2 (95/5) atmosphere for one hour. The final pellet has a diameter of 11.5 mm and a thickness of ~5 mm with porosity lower than 10%. A tapping was made in the edge of the pellet in order to connect a threaded Inconel 718 or nickel aluminium bronze alloy C63000 rod protected by an alumina based ceramic coating.

The structure of the as-milled and consolidated powders was determined by X-ray diffraction (XRD) analyses performed using a Bruker D8 diffractometer with a Cu k_α radiation. Micrographs of the materials were carried out in backscattered electron (BSE) mode using a JEOL JSM-6300F scanning electron microscope (SEM). Their chemical composition was determined by energy dispersive X-ray spectroscopy (EDS).

The high temperature oxidation tests were carried out using a thermogravimetric analyser (Thermax 500). Before experiment, the as-milled powders were sieved (20-75 microns) and heat treated at 1000°C under Ar-5%H_2 atmosphere. The oxidation experiments were then conducted at 700°C under Ar-20%O_2 for 20 h. After oxidation, the samples were analyzed by XRD.

Electrochemical tests were performed at 700°C under argon atmosphere using a two-electrode configuration cell controlled by a VMP3 multichannel potentiostat/galvanostat (BioLogic Instruments). More details on the cell geometry are presented elsewhere **[13]**. The cathode was a graphite rod (~13 cm^2 immersed in the electrolyte). The anode-cathode distance was 2.3 cm. The crucible containing the electrolyte was made of sintered alumina. The electrolyte composition was 50 wt.% AlF_3-45 wt.% KF-5 wt.% Al_2O_3. The alumina concentration was almost constant during the experiment because its consumption is compensated by the dissolution of the alumina crucible **[11]**. Electrolysis tests were performed at an anode current density of 0.5 A/cm^2 for 20 h. Before measurement, the anode was maintained above the electrolyte for 30 min and then immersed in the electrolyte at open circuit conditions for 10 min. After electrolysis, the electrodes were analyzed by SEM-EDS and XRD. The Cu, Ni and Fe contents in the produced aluminium were determined by neutron activation from Al samples corresponding to about 90 % of the amount of Al produced for 20 h of electrolysis. Before neutron analysis, the Al sample (in ball form) was flattened and polished in order to eliminate residual electrolyte on its surface. The determination of the Y content was not possible by neutron activation.

Results and discussion

1) Structure of the as-milled and consolidated powders

Figure 1A shows the XRD patterns of the as-milled $Cu_{65}Ni_{20}Fe_{15}$ and $(Cu_{65}Ni_{20}Fe_{15})_{95}Y_5$ powders. After 10h of milling, the characteristic diffraction peaks of pure Cu, Ni and Fe are no longer observed. In both cases, one series of peaks are clearly discernible, which corresponds to a face-centered-cubic (fcc) phase attributed to a solid solution of Cu(Ni,Fe) named γ-phase. For the $(Cu_{65}Ni_{20}Fe_{15})_{95}Y_5$ sample, two small additional peaks are perceptible at ~31° and ~82°, which can be attributed to the presence of unalloyed yttrium. The fact that Y atoms do not dissolve in the γ phase is also confirmed by the absence of any shift on the diffraction peaks of the γ phase. It can be explained by the large atomic radius of yttrium (1.78 Å) compared to that of copper, nickel and iron (1.28, 1.25 and 1.24 Å, respectively).

After the powder consolidation treatment **(Fig. 1B),** no decomposition of the γ phase is observed. Only a decrease of the full width at half maximum (FWHM) of the diffraction peaks of the γ phase is observed due to grain growth and strain release. On the basis of Williamson-Hall plots (not shown), the crystallite size is ~30 nm and the lattice strain is ~0.3 % for the consolidated samples compared to ~10 nm and ~0.8% before consolidation. In addition, a new set of diffraction peaks is visible in the ~29-36° region of the XRD pattern of the consolidated $(Cu_{65}Ni_{20}Fe_{15})_{95}Y_5$ whereas the diffraction peaks of pure Y are missing. These new diffraction peaks may be attributed to the formation of Y-Ni rich precipitates during the consolidation treatment, as confirmed by SEM-EDS observations (see hereafter).

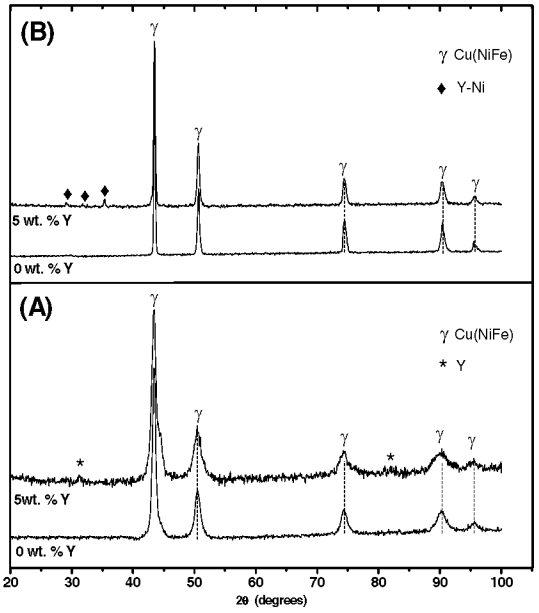

Fig. 1. XRD patterns of the $Cu_{65}Ni_{20}Fe_{15}$ and $(Cu_{65}Ni_{20}Fe_{15})_{95}Y_5$ powders in as-milled state (A) and after consolidation (B).

BSE micrograph of the consolidated $Cu_{65}Ni_{20}Fe_{15}$ sample (**Fig. 2A**) shows no apparent chemical segregation, confirming the efficiency of the mechanical alloying process for producing highly homogeneous Cu-Ni-Fe alloys. This strongly differs from what is observed on as-cast Cu-Ni-Fe alloys where the presence of micrometric Fe-Ni rich dendrites resulting from the alloy spinodal decomposition are clearly discernible **[14]**. BSE image of the consolidated $(Cu_{65}Ni_{20}Fe_{15})_{95}Y_5$ sample (**Fig. 2B**), supported by EDS analyses, confirms the presence of Y-Ni rich precipitates (dark grey areas) well distributed in the Cu(Ni,Fe) phase matrix (light grey areas). Their sizes are typically between 0.2 and 2 µm. Their atomic composition determined by EDS is close to Y_3Ni_2.

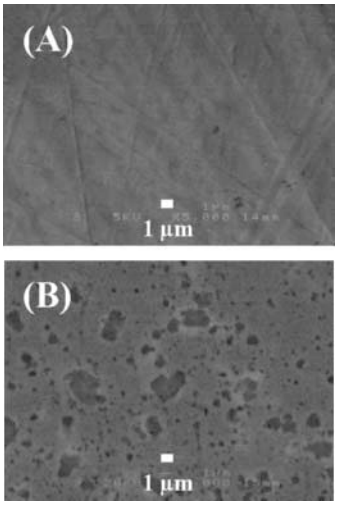

Fig.2. BSE images of the consolidated $Cu_{65}Ni_{20}Fe_{15}$ (A) and $(Cu_{65}Ni_{20}Fe_{15})_{95}Y_5$ (B) samples.

3) High-temperature oxidation behavior

Figure 3 shows the TGA curves performed at 700°C under 1 atm Ar:O_2 (80:20) for the $Cu_{65}Ni_{20}Fe_{15}$ and $(Cu_{65}Ni_{20}Fe_{15})_{95}Y_5$ powders. For $Cu_{65}Ni_{20}Fe_{15}$, a very rapid increase of the mass is observed during the first 4 hours of oxidation, which is mainly attributed to the formation of CuO. The oxidation rate drastically slows down for t > 4 h and it can be associated with the formation of $NiFe_2O_4$ through a solid state reaction between NiO and Fe_2O_3 **[10]**. After 17 h of oxidation, the mass gain reaches 28%. This gain corresponds to the total oxidation of the powder, assuming the formation of CuO, NiO and Fe_2O_3. Yttrium addition in the Cu-Ni-Fe alloy decreases drastically the alloy oxidation kinetics. Indeed, the rapid mass gain previously observed during the first hours of oxidation is not observed in the present case, which means that the formation of CuO is significantly slowed down. The mass gain reaches 15% after 17 h of oxidation.

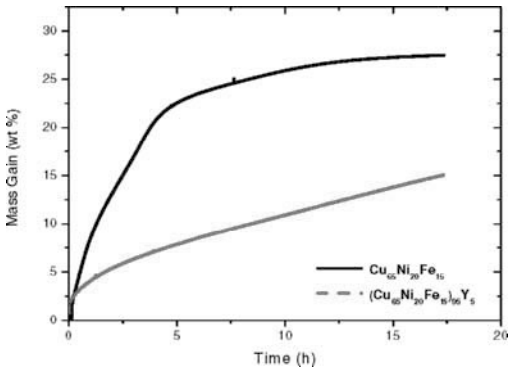

Fig.3. TGA curves of $Cu_{65}Ni_{20}Fe_{15}$ and $(Cu_{65}Ni_{20}Fe_{15})_{95}Y_5$ performed at 700°C under 1 atm Ar-20%O_2.

The XRD patterns of the samples after the oxidation test (**Fig. 4**) confirm the complete oxidation of $Cu_{65}Ni_{20}Fe_{15}$ to CuO and $NiFe_2O_4$. In contrast, the oxidation of $(Cu_{65}Ni_{20}Fe_{15})_{95}Y_5$ sample is incomplete since the peaks of the γ phase are clearly visible. The oxides are mainly CuO and $NiFe_2O_4$, but there is also some trace amount of Cu_2O and probably Y_2O_3 (peak at ~29°). Note that the presence of NiO cannot be excluded because their characteristic peaks closely overlap those of the $NiFe_2O_4$ phase.

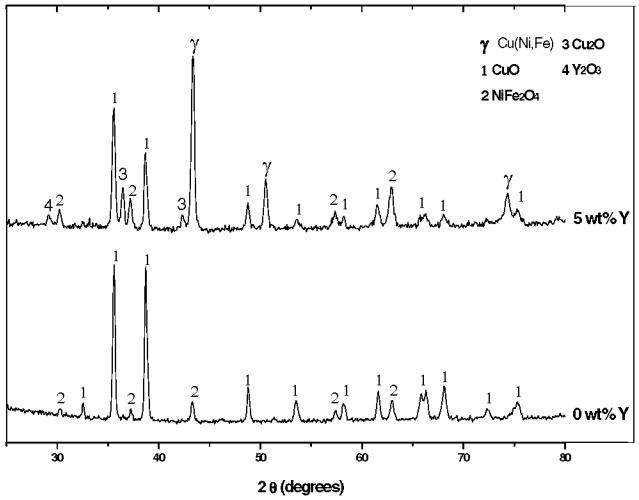

Fig.4. XRD patterns of $Cu_{65}Ni_{20}Fe_{15}$ and $(Cu_{65}Ni_{20}Fe_{15})_{95}Y_5$ samples after high temperature oxidation tests.

These results demonstrate that the Y addition has a significant positive effect on the high-temperature oxidation resistance of the Cu-Ni-Fe alloy. A possible explanation is that the presence of finely dispersed Y-Ni inclusions in the Cu-Ni-Fe matrix (**Fig. 2B**), resulting in the formation of Y_2O_3 precipitates, limits the outward diffusion of Cu in Cu oxides, inducing a lower alloy oxidation rate as shown in **Fig. 3**.

4) Aluminum electrolysis

Figure 5 shows the evolution of the cell voltage during Al electrolysis at I_{anode}= 0.5A/cm^2 in low-temperature (700°C) KF-AlF_3 electrolyte. No major difference can be observed between the two electrodes. The cell voltage at the $(Cu_{65}Ni_{20}Fe_{15})_{95}Y_5$ electrode (**Fig. 5B**) appears slightly more stable at around 4.0±0.1 V compared to 4.0±0.3 V for the $Cu_{65}Ni_{20}Fe_{15}$ electrode (**Fig. 5A**).

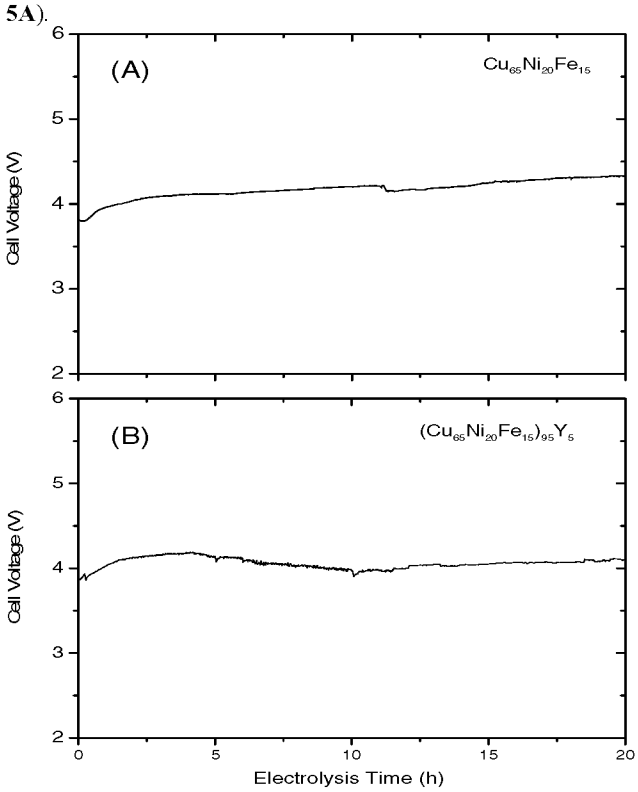

Fig.5. Cell voltage vs. electrolysis time at I_{anode} =0.5 A/cm^2 for $Cu_{65}Ni_{20}Fe_{15}$ (A) and $(Cu_{65}Ni_{20}Fe_{15})_{95}Y_5$ (B) electrodes.

A visual inspection of the two electrodes after 20 h of electrolysis does not show any evidence of degradation except for the presence of an oxide scale at the electrode surface. **Figure 6** shows the BSE cross-section images of the $Cu_{65}Ni_{20}Fe_{15}$ and $(Cu_{65}Ni_{20}Fe_{15})_{95}Y_5$ anodes after 20 h of electrolysis. The presence of an oxide scale is easily discernible, which has delaminated from the bulk alloy, probably due to the thermal shock when the electrode was taken out of the electrolyte. In both cases, the surface scale is composed of three main layers but their thickness and nature (determined from EDS and XRD analyses recorded after polishing the electrodes for different times, not shown) depend on the electrode composition. In the case of the $Cu_{65}Ni_{20}Fe_{15}$ anode (**Fig. 6A**), the outermost layer is a ~200 µm thick Cu_2O-rich scale resulting from the outward diffusion of Cu in Cu oxides. The intermediate layer (~150 µm in thickness)

consists mainly of $NiFe_2O_4$ which is formed from the internal oxidation of Fe and Ni with the subsequent formation of $NiFe_2O_4$ **[10]**. Near the bulk alloy, a non-continuous layer of FeF_2 (~100 µm in thickness) is observed, which was probably formed when the anode was immersed in the electrolyte at open circuit conditions for 10 min or during the first few minutes of electrolysis, *i.e.* when the protective oxide layer had not yet formed. For the $(Cu_{65}Ni_{20}Fe_{15})_{95}Y_5$ anode (**Fig. 6B**), the oxide scale is thinner with a total thickness of ~200 µm compared to ~350 µm for the $Cu_{65}Ni_{20}Fe_{15}$ anode. The outermost layer (~120 µm thick) is composed of $NiFe_2O_4$ with CuO and Fe_2O_3 inclusions. Underneath, a layer (~80 µm thick) consisting mainly of $NiFe_2O_4$ is present. Some yttrium oxide precipitates were also detected in this layer. Finally, the inner layer (~100 µm thick) is made up of FeF_2 inclusions inside the alloy matrix as observed for the $Cu_{65}Ni_{20}Fe_{15}$ anode. The fact that the oxide scale is thinner and poorer in Cu oxides at the $(Cu_{65}Ni_{20}Fe_{15})_{95}Y_5$ anode than at the $Cu_{65}Ni_{20}Fe_{15}$ anode confirms that the outward diffusion of Cu in Cu oxides is significantly slowed down. As discussed before, this may be attributed to the presence of finely dispersed Y-Ni precipitates in the Cu-Ni-Fe matrix, limiting the mobility of the Cu atoms. On the other hand, the Y-Ni precipitates may be unfavorable to the formation of $NiFe_2O_4$, which can explain the presence of a significant amount of Fe_2O_3 in the oxide scale.

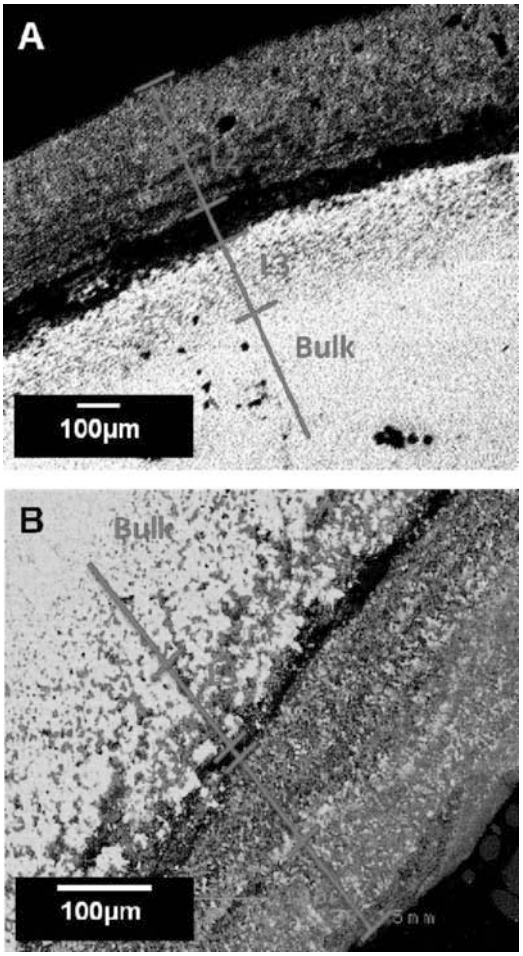

Fig 6. BSE cross section micrographs of $Cu_{65}Ni_{20}Fe_{15}$ (A) and $(Cu_{65}Ni_{20}Fe_{15})_{95}Y_5$ (B) anodes after 20 h of electrolysis.

The aluminum produced using the $(Cu_{65}Ni_{20}Fe_{15})_{95}Y_5$ electrode presents a lower Cu contamination (0.13 wt. %) than with the $Cu_{65}Ni_{20}Fe_{15}$ anode (0.39 wt. %). This agrees with the lower amount of Cu oxides on the surface for the Y-containing anode as shown previously. The Ni contamination is similar for both anodes (~0.12 wt%). Unfortunately, an increase in Fe contamination is observed with the $(Cu_{65}Ni_{20}Fe_{15})_{95}Y_5$ anode (0.32 vs 0.21 wt%), which can be related to the larger amount of iron oxides on the electrode surface layer as shown before. As a result, the improvement of the Al purity is small and may not be statistically significant (99.42 wt.% with $(Cu_{65}Ni_{20}Fe_{15})_{95}Y_5$ *vs.* 99.28 wt. % with $Cu_{65}Ni_{20}Fe_{15}$). Similar experiments should be repeated several times to confirm that these differences in impurity levels are statistically significant. For comparison, aluminum with a purity of 99.76 % was obtained with an $(Cu_{65}Ni_{20}Fe_{15})_{98.6}O_{1.4}$ anode **[11]**.

Conclusion

The influence of yttrium addition (5 wt. %) on the corrosion resistance of the mechanically alloyed $Cu_{65}Ni_{20}Fe_{15}$ anode for Al electrolysis in low-temperature KF-AlF_3 electrolyte was investigated. Y atoms do not dissolve in the Cu(Ni,Fe) phase with milling and they induce the formation of Y-Ni precipitates during the subsequent powder consolidation procedure. These inclusions have a positive influence on the alloy corrosion resistance by slowing down the outward diffusion of Cu in Cu oxides. However, its impact on the purity of the produced Al seems to be limited. Complementary study with different amounts of added Y is in progress to investigate this issue.

References

1. The Aluminum Association of Canada, *"2010 Sustainable development report"* (2011).
2. The Aluminum Association, *"Inert Anode Roadmap: A Framework for Technology Development"* (Washington, 1998).
3. I Galasiu, R. Galasiu and J. Thonstad, *"Inert Anodes for Aluminium Electrolysis"* (Aluminium-Verlag, Dusseldorf , 2007).
4. ASME Technical Working Group, *"Inert anode technologies report"* (U.S. Department of Energy, Office of Industrial Technologies, Washington, 1999).
5. J. Yang, D. Graczyk, C. Wunsch, and J.N. Hryn, *"Alumina solubility in KF-AlF3-based low-temperature electrolyte system"* Light Metals 2007 (TMS, Warrendale, Pa), 537-541.
6. J. Yang, J.N. Hryn, and G.K. Krumdick, *"Aluminum electrolysis tests with inert anodes in KF-AlF3-based electrolystes"* Light Metals 2006 (TMS, Warrendale, Pa), 421-424
7. J. Yang, J. N. Hryn, B. R. Davis, A. Roy, G. K. Krumdick and J. A. Pomykala Jr, *"New Opportunities for Aluminum Electrolysis with Metal Anodes in a Low Temperature Electrolyte System"* Light Metals 2004 (TMS, Warrendale, Pa), 321-326.
8. T.R. Beck, and R.J. Brooks "*Non-consumable anode and lining for aluminium electrolytic reduction cell"* US patent 5,284,562 (1994).
9. T.R. Beck, C.M. MacRae, and N.C. Wilson, *"Metal anode performance in low-temperature electrolytes for aluminum production"*, Metall. Mat. Trans. B, 42 (2011) 807-813
10. S. Helle, M. Pedron, B. Assouli, B. Davis, D. Guay, and L. Roué, *"Structure and high-temperature oxidation behavior of Cu-Ni-Fe based alloys prepared by high-energy ball milling for*

application as inert anodes for aluminum electrolysis" Corros. Sci., 52 (2010) 3348-3355.
11. S. Helle, M. Tresse, B. Davis, D. Guay, and L. Roué, *"Mechanically alloyed Cu-Al-Ni-O based materials as oxygen-evolving anodes for aluminum electrolysis"*, J. Electrochem. Soc., 159 (2012) E62-E68.
12. F. Riffard, H. Buscail, E. Caudron, R. Cueff, C. Issartel, and S. Perrier, "*Effect of yttrium addition by sol–gel coating and ion implantation on the high temperature oxidation behaviour of the 304 steel",* Appl. Surf. Sc., 199 (2002) 107-122.
13. S. Helle, B. Davis, D. Guay and L. Roué, "*Electrolytic production of aluminum using mechanically alloyed Cu-Al-Ni-Fe based materials as inert anodes",* J. Electrochem. Soc., 157 (2010) E173-E179
14. I. Gallino, M.E. Kassner, and R. Bush, *"Oxidation and corrosion of highly alloyed Cu–Fe–Ni as inert anode material for aluminum electrowinning in as-cast and homogenized conditions*" Corros. Sci., 63 (2012) 293-303.